

or spontaneous symmetry breaking [17, 33], due to the extensive number of local degeneracies dictated by the symmetry group. Take the random XXZ chain for example, the symmetry group $U(1) \rtimes \mathbb{Z}_2$ is a product of the spin-Z conservation and the spin-flipping \mathbb{Z}_2 symmetry. Following the argument given in Ref. [34], the symmetric marginal MBL state, if possible, should be characterized by a set of quasi-LIOM, which form irreducible representations of the $U(1) \rtimes \mathbb{Z}_2$ symmetry group. However, the $U(1) \rtimes \mathbb{Z}_2$ symmetry enforces a local degeneracy between states of opposite spin-Z for every quasi-LIOM. As a result, the finite energy density eigenstates in the many-body spectrum are all exponentially degenerate. Because the extensive degeneracy is unstable to quantum fluctuations, the eigenstates must either localize to symmetry breaking spin glass states or thermalize, both of which destroy the quantum criticality.

So to explore marginal MBL phases in 1D spin systems, we must sufficiently break the symmetry to remove all local degeneracies. This motivates us to look at the XYZ spin chain, with independently random XX, YY and ZZ couplings on each bond. The symmetry is broken down to \mathbb{Z}_2^2 , such that local degeneracies are completely removed (because \mathbb{Z}_2^2 has no irreducible representations beyond the one-dimensional representations). Therefore, marginal MBL states of the XYZ spin chain can be stable at finite energy density against thermalization and spontaneous symmetry breaking as long as the disorder is strong enough. Due to the discrete \mathbb{Z}_2^2 symmetry, at each RG step there is only one unique leading energy scale term that bifurcates the spectrum. This is precisely the type of model that SBRG was designed to target.

Apart from the above symmetry considerations, strong disorder is another key ingredient to keep the marginal MBL states from thermalizing. We introduce the standard deviation of the logarithmic scale of the coupling strengths

$$\Gamma = \text{std}(\ln |J|) \quad (1)$$

(where J appears as coefficients in the Hamiltonian, e.g. Eq. (2)) to compare the strength of three often used disorder distributions: uniform, Gaussian, and the power-law distribution which will be used in this work. Physically, Γ describes how much different couplings are separated in their energy scales. Well separated energy scales in the large Γ limit suppress the resonance between energy levels, and hence hinders thermalization. Our finite-size exact diagonalization (ED) study (Appendix D) indicates that $\Gamma \simeq 1$ is not sufficient to stabilize the marginal MBL phases in the XYZ model against thermalization. Therefore, instead of drawing the coupling strengths from uniform distributions ($\Gamma = 1$) or Gaussian distributions ($\Gamma \approx 1.1$), we need to take power-law distributions (Appendix C1) whose Γ can be tuned all the way to infinity. We

will typically take $\Gamma = 4$ as the initial distribution in our calculation. SBRG is well-suited to study such strong disorder spin systems, as the SBRG algorithm is asymptotically accurate in the large Γ limit.

In the following, we will first introduce the model and present the phase diagram. Then we focus on a high symmetry line in the phase diagram, and investigate the MBL spin glass phase and marginal MBL critical phase in detail. In particular, we calculate the entanglement entropy, Edwards-Anderson correlator and long-range mutual information. We found that the marginal MBL critical line is characterized by an effective central charge $c' = \ln 2$. Our data also suggest continuously varying exponents along the critical line.

II. XYZ SPIN CHAIN MODEL

We study the XYZ spin chain with large disorder and periodic boundary conditions. The Hamiltonian is given by

$$H = \sum_{i=1}^L \sum_{\mu=x,y,z} J_{i,\mu} \sigma_i^\mu \sigma_{i+1}^\mu. \quad (2)$$

σ_i^μ with $\mu = 1, 2, 3$ are Pauli matrix operators on lattice site i of a 1d chain of length L . The couplings $J_{i,\mu} \in [0, J_\mu]$ are randomly drawn from a power-law distribution

$$\text{PDF}(J_{i,\mu}) = \frac{1}{\Gamma J_{i,\mu}} \left(\frac{J_{i,\mu}}{J_\mu} \right)^{1/\Gamma}, \quad (3)$$

where $0 < \Gamma < \infty$ (see Eq. (1)) controls the disorder strength (for details see Appendix C1). Equivalently, $J_{i,\mu}^{1/\Gamma} \in [0, J_\mu^{1/\Gamma}]$ is uniformly distributed. For later convenience, we define

$$\tilde{J}_\mu \equiv J_\mu^{1/\Gamma}, \quad (4)$$

and take $\tilde{J}_\mu = \tilde{J}_x, \tilde{J}_y, \tilde{J}_z$ as our primary tuning parameters (see Appendix C2 for an explanation). We will be interested in the entire energy spectrum of this model, as opposed to just the low energy states.

Beside the exact global symmetry \mathbb{Z}_2^2 , the model also has some statistical symmetries, which are valid only in the statistical sense over the ensemble of the disordered Hamiltonians. When $J_x = J_y$ (and similarly for $J_y = J_z$ and $J_z = J_x$), the *distribution* of Hamiltonians H has a \mathbb{Z}_2 symmetry which swaps $J_{i,x} \leftrightarrow J_{i,y}$. When $J_x = J_y = J_z$, the distribution of Hamiltonians has an S_3 permutation symmetry which permutes $J_{i,x} \leftrightarrow J_{i,y} \leftrightarrow J_{i,z}$. For any J_μ , the distribution of Hamiltonians also has translation symmetry. Imposing these statistical symmetries can be used to easily fine tune the XYZ model to its critical phases.

In the existing literature, the RSRG-X approach [13, 15, 17, 33] has been successfully applied to analyze

various marginal MBL phases in disordered spin systems. However, it is challenging to apply the traditional closed-form RSRG-X analysis to the XYZ model, even near the free fermion soluble points (such as $J_x = J_y$ and $J_z \rightarrow 0$). At the free fermion soluble point, the spin system can be mapped to two independent Majorana chains with uncorrelated randomness, which allows the standard bond decimation RG scheme to be applied independently on each chain. However, once the fermion interactions (J_z terms) are introduced to the system, the two Majorana chains are coupled together as a ladder lattice. The independent bond decimation on both chains will quickly distort the ladder lattice and generate complicated configurations of multi-fermion interactions, which can not be tracked in closed-form. Therefore, we turn to the numerical approach of SBRG, which can keep track of all orders of multi-fermion interactions generated under the RG flow.

In the following, we will study the XYZ model by applying SBRG. We will show results for $\Gamma = 4$ initial randomness, for which SBRG agrees well with exact diagonalization on small lattices (data not shown in this paper), and our approximations appear to be safe (see Appendix B 1 and D, and Sec. III B). We will also limit our system sizes to $L \leq 256$ because our current implementation of SBRG does not produce accurate results for larger system sizes on the critical lines of the XYZ model.

III. PHASE DIAGRAM

A. Spin Glass Phases

With large disorder and at finite energy density, there are three spin glass phases (Fig. 1). We find that if \tilde{J}_z is the largest coupling constant (i.e. $\tilde{J}_z > \tilde{J}_x$ and $\tilde{J}_z > \tilde{J}_y$), then the system is in an MBL spin glass phase where the correlator $\sigma_i^z \sigma_j^z$ shows long range glassy behavior. That is, $\sigma_i^z \sigma_j^z$ develops a finite overlap with products of the local integrals of motion (LIOM) τ^z s of the MBL phase (see Eq. (A1) in Appendix A), and is thus roughly conserved. This finite overlap results in an Edwards-Anderson correlator that asymptotes to a nonzero constant at large distance, which we take to be the primary signature of a spin glass phase.

B. Critical Phases

With sufficiently strong disorder, the spin glass phases appear to be separated by a critical lines (e.g. $\tilde{J}_z \leq \tilde{J}_x = \tilde{J}_y$) consisting of marginal MBL phases, which is evidenced by the fact that the entanglement entropy diverges logarithmically (Fig. 4) in this phase. In Fig. 2 we provide evidence that the critical ($\tilde{J}_z \leq \tilde{J}_x = \tilde{J}_y$)

entanglement entropy S_E vs coupling constants

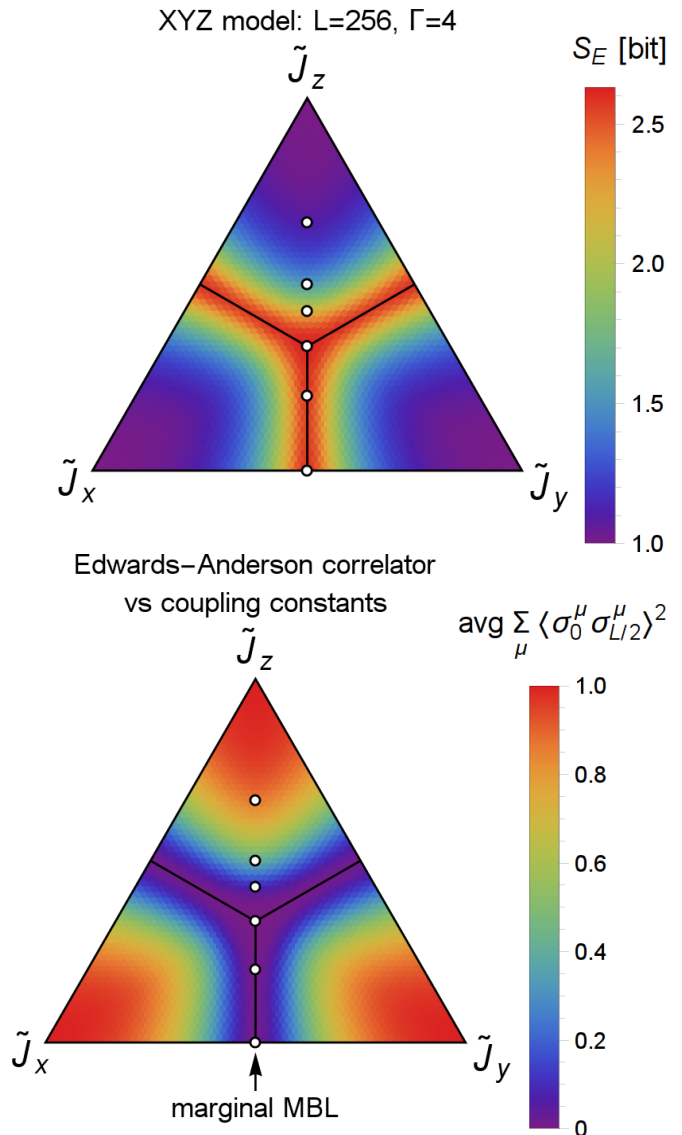


FIG. 1: Ternary plot of the disorder and energy averaged entanglement entropy S_E [bit] ($\equiv S_E/\ln 2$) (Eq. (6)) of a subsystem of length $L/2$ (top) and Edwards-Anderson correlator (Eq. (9)) (bottom) vs coupling constants ($0 < \tilde{J}_{x,y,z} < 1$) for the XYZ spin chain of length $L = 256$. We use this plot to sketch the phase diagram. When $\tilde{J}_z > \max(\tilde{J}_x, \tilde{J}_y)$, the system is in a \mathbb{Z}_2 spin glass state. When $\tilde{J}_z < \tilde{J}_x = \tilde{J}_y$, the system is in a marginal MBL phase. (The other phases are given by permutations of x, y, z .) The white dots correspond to the points in the phase diagram that are shown in Fig. 4, 5, 7.

to spin glass ($\tilde{J}_z > \tilde{J}_x = \tilde{J}_y$) phase transition is continuous and occurs exactly at $J_x = J_y = J_z$ by showing evidence that the long-range spin glass Edwards-Anderson correlator is zero when $\tilde{J}_z \leq \tilde{J}_x = \tilde{J}_y$ and increases continuously for $\tilde{J}_z > \tilde{J}_x = \tilde{J}_y$. An example of how the LIOM look in this phase is shown in Fig. 11.

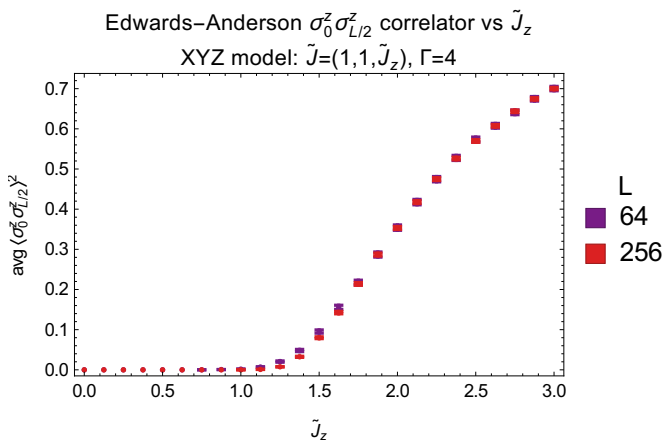


FIG. 2: Disorder and energy averaged Edwards-Anderson correlator (Eq. (9)) at separation $x = L/2$ vs \tilde{J}_z for different system sizes L in the XYZ spin chain with $\tilde{J}_x = \tilde{J}_y = 1$. In the critical phase, the Edwards-Anderson correlator decays algebraically to zero; while in the spin glass phase, the Edwards-Anderson correlator asymptotes to a constant. Furthermore, as one tunes \tilde{J}_z from the critical phase to the spin glass phase, the Edwards-Anderson correlator becomes nonzero continuously at $\tilde{J}_z = 1$, indicating that this marks the location of a continuous phase transition. (error bar details: [35])

Marginal MBL vs Thermal

With sufficiently large disorder, SBRG depicts the critical phase as marginally MBL as SBRG finds a logarithmically diverging entanglement entropy in this phase. However, SBRG is not capable of describing thermalization, and so one should worry that resonance effects may thermalize the critical phase. Indeed, the instability of marginal MBL phase to thermalization has been demonstrated in other 1D spin models. [17, 33] Thus, it is crucial to check the approximations made by SBRG, in order to verify that an exact RG does not flow toward thermalization. In Appendix D we do a brief exact diagonalization study to check that with strong disorder, the system is not thermal. Below, we will study the evidence against thermalization by using SBRG.

The core approximation made by SBRG is the validity of the second order perturbation theory used by each RG step. This and other approximations are explained in detail and accounted for in Appendix B 1. However, even though these approximations are controlled by strong disorder, one could still worry that errors may build up during the RG flow and cause SBRG to incorrectly depict the critical phase as a marginal MBL phase, even if the critical phase is actually thermal.

At intermediate RG steps, a cluster of n “LIOM” could resonate and become thermalized by an off-diagonal term that mixes (i.e. anticommutes with) them if the energy of the off-diagonal term ε_{mix} is larger than the smallest

energy difference ΔE of the n “LIOM”: i.e. if $\varepsilon_{\text{mix}} > \Delta E$. The verified assumptions Eq. (B2) and B3 imply that this rarely occurs for small n . However, one might worry that large clusters of n “LIOM” could be thermalized by rare off-diagonal terms [36]. But a cluster of n LIOM will describe 2^n states, and thus typically have a smallest energy level spacing equal to $\Delta E \sim 2^{-n}$ (because our model has a small symmetry, there is no symmetry protected degeneracy in this cluster); while below we argue that off-diagonal terms at intermediate RG steps will have energies of order $\varepsilon_{\text{mix}} \lesssim e^{-\Gamma n}$, which is much smaller than $\Delta E \sim 2^{-n}$ for large disorder Γ . Thus, $\varepsilon_{\text{mix}} \ll \Delta E$ and so it seems unlikely that enough clusters of n “LIOM” could resonate to thermalize the system.

To show that $\varepsilon_{\text{mix}} \lesssim e^{-\Gamma n}$, we note that at intermediate RG steps, the energies of off-diagonal terms mixing n “LIOM” should be roughly bounded by the the largest n -body coefficient $h_{\text{max}}^{(n)}$ of the effective Hamiltonian H_{eff} (Eq. (A1)): $\varepsilon_{\text{mix}} \lesssim h_{\text{max}}^{(n)}$. And in Fig. 3 we show that $h_{\text{max}}^{(n)}$ decays exponentially with Γn :

$$h_{\text{max}}^{(n)} \equiv \max_{ij\dots} |h_{ij\dots}^{(n)}| \sim e^{-\Gamma n} \quad (5)$$

Thus $\varepsilon_{\text{mix}} \lesssim h_{\text{max}}^{(n)} \sim e^{-\Gamma n}$.

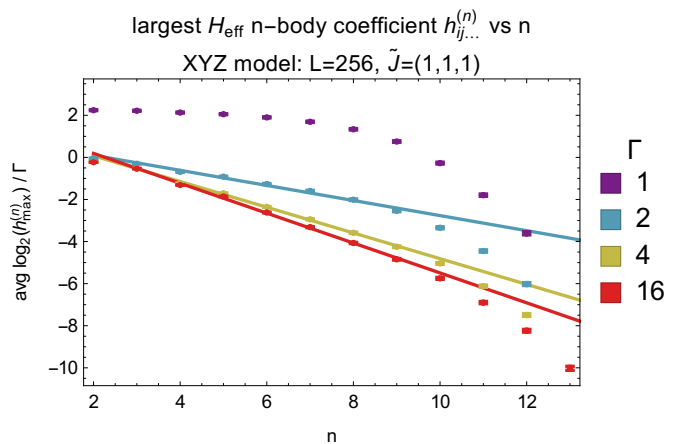


FIG. 3: Disorder average of $\log_2(h_{\text{max}}^{(n)})/\Gamma$ vs n for different amounts of disorder Γ where $h_{\text{max}}^{(n)} \equiv \max_{ij\dots} |h_{ij\dots}^{(n)}|$ (Eq. (5)) is the largest n -body coefficient $h_{\text{max}}^{(n)}$ of the effective Hamiltonian H_{eff} at the critical point $\tilde{J}_x = \tilde{J}_y = \tilde{J}_z = 1$. As the disorder Γ increases, the data converges to a single straight line. For large n , the data drops below the linear fit line. This is expected to be an artifact of dropping terms in SBRG (see Sec. B3 for details). Solving for $h_{\text{max}}^{(n)}$ gives $h_{\text{max}}^{(n)} \sim e^{-\Gamma n}$ as in Eq. (5), which completes our argument that the critical line is marginally MBL. (error bar details: [35])

IV. ENTANGLEMENT ENTROPY

The entanglement entropy is a useful tool to probe quantum phase transitions from the entanglement patterns of the many-body state, and has the nice property that one does not have to pick the right order parameter. Instead, one only has to choose a useful subsystem geometry. SBRG can efficiently calculate [1] entanglement entropies using the stabilizer rank algorithm introduced by Ref. [37].

The entanglement entropy S_E of a subsystem A for a wavefunction $|\psi\rangle$ is defined to be

$$S_E(A) \equiv -\text{Tr}[\rho_A \ln \rho_A] \quad (6)$$

$$\rho_A = \text{Tr}_{\bar{A}} |\psi\rangle\langle\psi|$$

where $\text{Tr}_{\bar{A}}$ means that degrees of freedom not in A are traced out. The disorder configuration (δ) and energy (E) averaged entanglement entropy is then

$$\text{avg } S_E(A) \equiv \frac{1}{N_\delta} \sum_{\delta} \frac{1}{N_E} \sum_E S_E(A) \quad (7)$$

where ψ and thus ρ_A in Eq. (6) depend on δ and E . We average over all energy eigenstates because we're interested in the entire spectrum of states. Additionally, in the strong disorder limit, the LIOM take the form of products of Pauli matrices, and the eigenstates of these LIOM (and the Hamiltonian) all have the same entanglement entropies. However, this is only a special feature of Pauli-like LIOM in the strong disorder limit. Away from the strong disorder limit, the LIOM will be further dressed by higher order corrections, such that different eigenstates will not have identical entanglement structures. Nevertheless, the difference of entanglement entropies across the spectrum will be relatively small in the strong disorder regime. So we will neglect the spectral dependence, and consider the energy averaged entanglement entropy.

First, we will take the subsystem A to be a line segment of length ℓ . We will be interested in how the entanglement entropy scales as the subsystem length ℓ increases. Later, in Sec. VI we will use more complicated subsystem geometries in order to study the long range mutual information of the XYZ model. As shown in Fig. 4, in the spin glass phases, the entanglement entropy S_E asymptotes to a constant with increasing subsystem length ℓ since it is a short range correlated phase. Furthermore, $S_E \geq \ln 2$ due to the spin glass order. These results can be understood deep in the spin glass phase via the LIOM in Eq. (E1) from the stabilizer rank algorithm. [1, 37] See Appendix E for details.

In the critical phases, the entanglement entropy S_E appears to diverge logarithmically with subsystem length

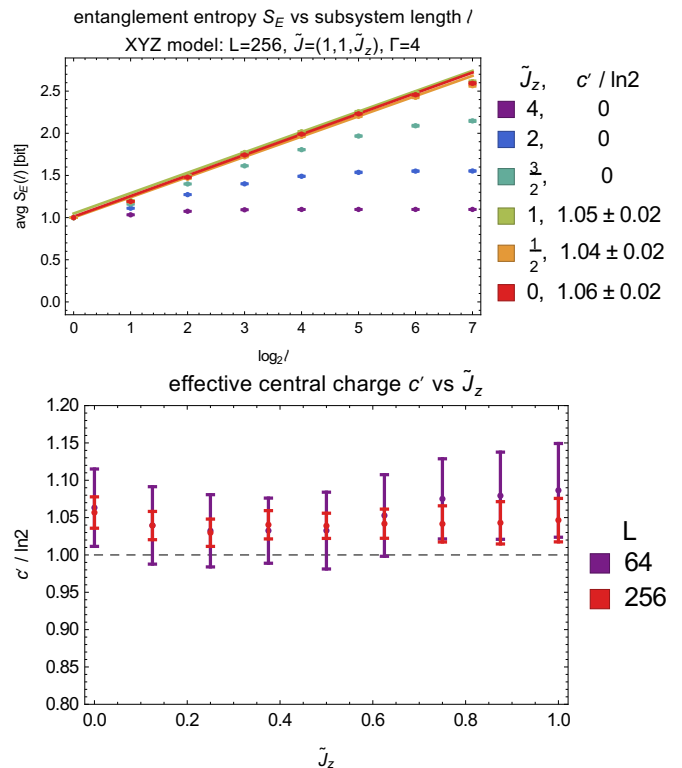


FIG. 4: **(top)** Disorder and energy averaged entanglement entropy S_E [bit] ($\equiv S_E / \ln 2$) (Eq. (6)) vs subsystem length ℓ for different \tilde{J}_z in the XYZ spin chain with $\tilde{J}_x = \tilde{J}_y = 1$ and system size $L = 256$. When $\tilde{J}_z > 1$, the system is a spin glass and the entanglement entropy follows an area law for large subsystems. When \tilde{J}_z is only slightly larger than 1, e.g. $\tilde{J}_z = 3/2$, there appears to be large finite size effects. When $\tilde{J}_z \leq 1$, the system is critical and the entanglement entropy follows a log law $S_E(\ell) \sim \frac{c'}{3} \ln \ell$, and the effective central charge c' is estimated using the slope of the fit to the $\ell = \frac{1}{2}\sqrt{L}, \sqrt{L}, 2\sqrt{L}$ data points. **(bottom)** Effective central charge c' (Eq. (8)) vs \tilde{J}_z for different system sizes L in the XYZ spin chain with $\tilde{J}_x = \tilde{J}_y = 1$. For all $\tilde{J}_z < 1$, the effective central charge appears to be consistent with $c' = c \ln 2$ [38] where $c = 1$ is the central charge without disorder. (error bar details: [35])

ℓ (Fig. 4):

$$S_E(\ell) = \frac{c'}{3} \ln \ell \quad (8)$$

$$c' = \ln 2$$

The constant c' is the effective central charge, which is postulated to be related to the central charge c without disorder by $c' = c \ln 2$ [38] (for Ising and Heisenberg types of models). Without disorder, the XYZ model has $c = 1$ in the critical phase, and so we expect and observe $c' = \ln 2$ in our disordered model (Fig. 4). The logarithmically diverging entanglement entropy in Eq. (8) is a result of the LIOM becoming nonlocal (see Fig. 11). This causes more LIOM to be cut by the subsystem A and enter the entanglement entropy equation Eq. (E2).

V. EDWARDS-ANDERSON CORRELATOR

A common approach to characterize glassy order is the Edwards-Anderson correlator. The disorder and energy averaged Edwards-Anderson spin glass correlator of $\sigma_0^\mu \sigma_x^\mu$ is defined to be

$$\text{avg}\langle\sigma_0^\mu\sigma_x^\mu\rangle^2 \equiv \frac{1}{N_\delta} \sum_\delta \frac{1}{N_E} \sum_E \langle E | \sigma_0^\mu \sigma_x^\mu | E \rangle_\delta^2 \quad (9)$$

It is the average of the square of $\langle\sigma_0^\mu\sigma_x^\mu\rangle$ over disorder configurations (δ) and energies (E). σ_0^μ and σ_x^μ are Pauli matrices at lattice sites 0 and x , respectively. We average over all energy eigenstates because we're interested in the entire spectrum of states. Additionally, in the strong disorder limit, the LIOM take the form of products of Pauli matrices, and the eigenstates of these LIOM (and the Hamiltonian) all have the same Edwards-Anderson Correlators.

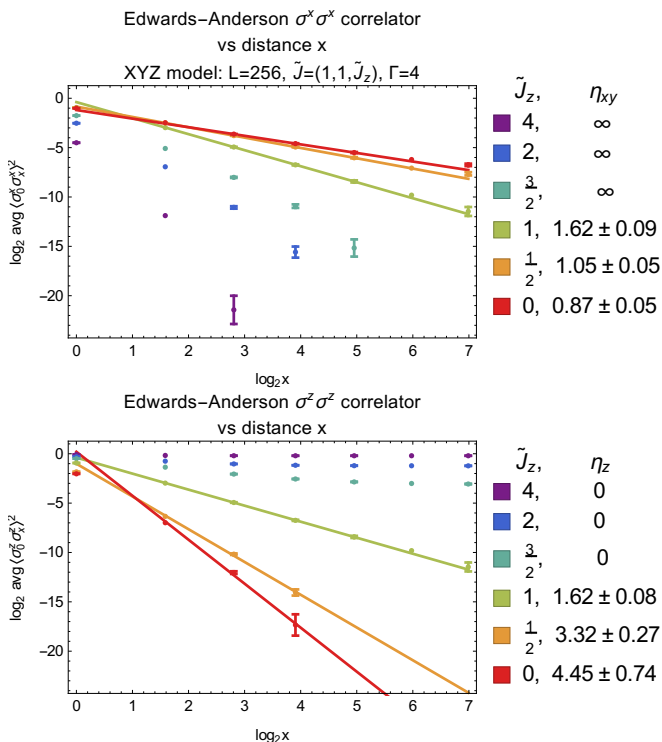


FIG. 5: Disorder and energy averaged Edwards-Anderson $\sigma^x \sigma^x$ (top) and $\sigma^z \sigma^z$ (bottom) correlators (Eq. (9)) vs distance x for different \tilde{J}_z in the XYZ spin chain with $\tilde{J}_x = \tilde{J}_y = 1$ and system size $L = 256$. When $\tilde{J}_z > 1$, the system is a $\sigma^z \sigma^z$ spin glass phase, and the $\sigma^x \sigma^x$ correlator decays exponentially while the $\sigma^z \sigma^z$ correlator asymptotes to a constant. When \tilde{J}_z is only slightly larger than 1, e.g. $\tilde{J}_z = 3/2$, there appears to be moderate finite size effects. When $\tilde{J}_z < 1$, the system is critical with power law $\sigma^\mu \sigma^\mu$ correlators (μ summation not implied) with critical exponents η_{xy} and η_z (Eq. (10), Fig. 6), which were calculated using the slope of the fit to the $x = \frac{1}{2}\sqrt{L} - 1, \sqrt{L} - 1, 2\sqrt{L} - 1$ data points. (error bar details: [35])

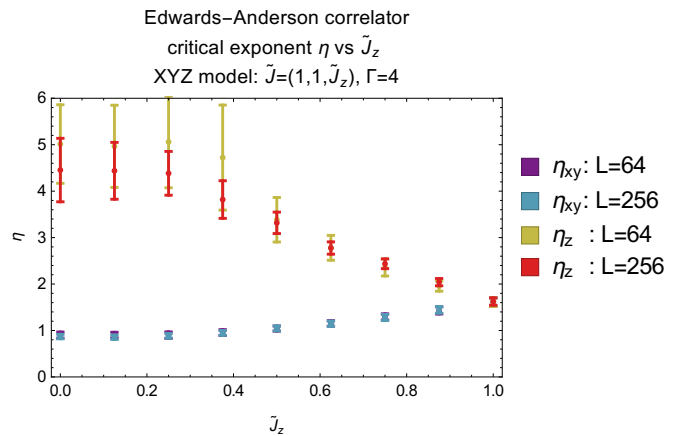


FIG. 6: Critical exponents η_{xy} and η_z (Eq. (10)) vs \tilde{J}_z with $\tilde{J}_x = \tilde{J}_y = 1$ for the XYZ spin chain of various system sizes L . η_{xy} (η_z) appears to increase (decrease) continuously as \tilde{J}_z increases. At least for $\tilde{J}_z > 1/2$, we do not expect the continuously varying exponents to be a result of finite size effects because η shows very little system size dependence in the above plot. The critical exponents were calculated as shown in Fig. 5. (error bar details: [35])

If $\tilde{J}_z > \tilde{J}_x$ and $\tilde{J}_z > \tilde{J}_y$, the system is in a $\sigma^z \sigma^z$ spin glass phase and the $\sigma^z \sigma^z$ Edwards-Anderson correlator (Eq. (9)) asymptotes to a constant for large distance x (with exponentially small corrections) (Fig. 5). Physically, this implies that $\sigma_i^z \sigma_j^z$ has developed a finite overlap with products of the local integrals of motion (LIOM) (Eq. (A1)) of the MBL phase, and is thus roughly conserved. However, the $\sigma^x \sigma^x$ and $\sigma^y \sigma^y$ correlators decay exponentially with distance x , as expected.

When $\tilde{J}_z < \tilde{J}_x = \tilde{J}_y$, the system is in a marginal MBL critical phase between $\sigma^x \sigma^x$ and $\sigma^y \sigma^y$ spin glasses (Fig. 1). The spin configuration in the marginal MBL state is dominated by nested domains of $\sigma^x \sigma^x$ and $\sigma^y \sigma^y$ Ising spin glass orders. The domains have fractal structures throughout the lattice, leading to the power-law decay of $\sigma^\mu \sigma^\mu$ Edwards-Anderson correlators (μ summation not implied) with critical exponents η_{xy} and η_z (Fig. 6):

$$\begin{aligned} \text{avg}\langle\sigma_0^x\sigma_x^x\rangle^2 &= \text{avg}\langle\sigma_0^y\sigma_x^y\rangle^2 \sim x^{-\eta_{xy}} \\ \text{avg}\langle\sigma_0^z\sigma_x^z\rangle^2 &\sim x^{-\eta_z} \end{aligned} \quad (10)$$

Unlike the effective central charge c' (Eq. (8)) which remains fixed, η_{xy} (η_z) appears to increase (decrease) continuously with increasing \tilde{J}_z . The power-law decay of $\sigma^z \sigma^z$ can be understood in the limit $J_z = 0$, where the system can be mapped to two independent free random Majorana fermion chains.

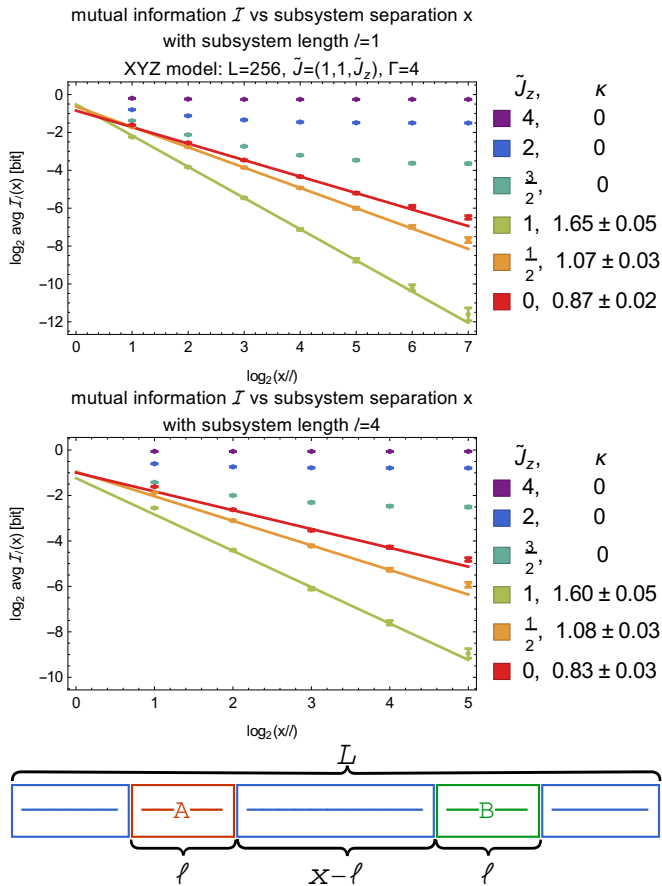


FIG. 7: Disorder and energy averaged long range mutual information (LRMI) \mathcal{I} of two subsystems (of length $\ell = 1$ (top) and $\ell = 4$ (middle)) vs subsystem separation x for different \tilde{J}_z in the XYZ spin chain with $\tilde{J}_x = \tilde{J}_y = 1$ and system size $L = 256$. Subsystem length ℓ and separation x are defined as shown in the bottom diagram. When $\tilde{J}_z > 1$, the system is in a spin glass phase, and the LRMI asymptotes to a constant. When \tilde{J}_z is only slightly larger than 1, e.g. $\tilde{J}_z = 3/2$, there appears to be moderate finite size effects. When $\tilde{J}_z \leq 1$, the system is in a marginal MBL phase, and the LRMI decays according to a power law with a critical exponent κ : $\mathcal{I}_\ell(x) \sim (x/\ell)^{-\kappa}$. The critical exponent κ does not appear to depend on the subsystem length ℓ , but it does appear to increase continuously with \tilde{J}_z , unlike the effective central charge c' which remains fixed (Fig. 4). If the above plots were drawn on top of each other, the critical $\tilde{J}_z \leq 1$ data would very nearly overlap, which implies that changing ℓ just rescales x as one would expect in a scale invariant system: $\mathcal{I}_\ell(x/\ell) \approx \mathcal{I}_{\ell'}(x/\ell')$. (error bar details: [35])

VI. LONG RANGE MUTUAL INFORMATION

In Sec. IV we used the entanglement entropy to diagnose the critical phase as a marginal MBL phase due to its logarithmically diverging entanglement entropy (Eq. (8)). However, only studying the asymptotics of the entanglement entropy $S_E(\ell)$ for large connected subsystem has some limitations. For example, $S_E(\ell)$

can not firmly distinguish a trivial phase from a spin glass, since both just asymptote to a constant. Instead of studying the entanglement entropy of just a single connected subsystem, it has been proposed to study the long range mutual information (LRMI) between two disconnected subsystems with large separation [2]. The mutual information \mathcal{I} between two non-overlapping subsystems A and B is defined to be

$$\mathcal{I}(A, B) = S_E(A) + S_E(B) - S_E(A \cup B) \quad (11)$$

We will take subsystems A and B to be lines of length ℓ with separation given by x as shown in Fig. 7 (bottom). We will be interested in the $L = \infty$ limit of the asymptotics of the LRMI $\mathcal{I}_\ell(x)$ as the separation x tends to infinity while the subsystem length ℓ is held fixed. Since the mutual information is also an upper bound of correlation functions, in principle, the mutual information should decay slower than any correlation function.

In a direct product state with no spin glass order (which doesn't exist in the XYZ model), far apart regions share little entanglement, and thus the LRMI should decay exponentially. In a spin glass phase there is long range glassy order, and the LRMI asymptotes to a constant (Fig. 7). Thus, LRMI can easily distinguish a trivial phase from a spin glass phase. This fact could be very useful in more complicated models where finding the right order parameter is difficult. Finally, in a critical phase in any dimension, the LRMI is expected to decay according to a power law with some critical exponent κ : $\mathcal{I}_\ell(x) \sim (x/\ell)^{-\kappa}$. In the XYZ model, a power law is indeed observed (Fig. 7). Since the mutual information should not decay faster than the correlation functions, we at least expect $\kappa \leq \min(\eta_{xy}, \eta_z)$, which is also verified within the numerical error. The critical exponent κ does not seem to depend on the subsystem length ℓ ; but κ does appear to increase continuously with \tilde{J}_z , unlike the effective central charge c' which remains fixed. Thus, the LRMI can efficiently tell if a phase is a trivial, spin glass, or marginal MBL critical phase; and works as expected in the XYZ model (Fig. 7).

VII. CONCLUSION

In conclusion, we have studied the XYZ spin chain with independently random XX, YY, and ZZ couplings on each bond. Unlike the random XXZ or Heisenberg models, the XYZ model breaks the continuous spin rotational symmetry down to the discrete \mathbb{Z}_2^2 symmetry, such that the quantum phase transitions between different symmetry-breaking spin glass phases can persist to finite energy density as marginal MBL critical lines. We use the SBRG numerical method to calculate the entanglement entropy, Edwards-Anderson correlator, and long-range mutual information. In the MBL spin

glass phase, the entanglement entropy follows the area-law scaling and quickly saturates to a value of $S_E \geq \ln 2$. Both the Edwards-Anderson correlator and the long-range mutual information exhibit long-range behavior, demonstrating spin glass order. Along the marginal MBL critical line, the entanglement entropy follows the logarithmic scaling $S_E(\ell) = (c'/3) \ln \ell$, with a fixed effective central charge $c' = \ln 2$. Both the Edwards-Anderson correlator and the long-range mutual information decays in a power-law, and the critical exponents varies continuously along the marginal MBL line.

We acknowledge helpful discussions with David Huse and Andrew Potter. In particular, Appendix D resulted from comments from David Huse. The authors are supported by David and Lucile Packard foundation and NSF Grant No. DMR-1151208.

-
- [1] Y.-Z. You, X.-L. Qi, and C. Xu, ArXiv e-prints (2015), 1508.03635.
- [2] C.-M. Jian, I. H. Kim, and X.-L. Qi, arXiv:1508.07006 (2015).
- [3] S. Sachdev, *Quantum Phase Transitions* (Cambridge University Press, 2011), 2nd ed., ISBN 9780521514682.
- [4] J. M. Deutsch, Phys. Rev. A **43**, 2046 (1991).
- [5] M. Srednicki, Phys. Rev. E **50**, 888 (1994).
- [6] M. Rigol, V. Dunjko, and M. Olshanii, Nature (London) **452**, 854 (2008), 0708.1324.
- [7] I. V. Gornyi, A. D. Mirlin, and D. G. Polyakov, Physical Review Letters **95**, 206603 (2005), cond-mat/0506411.
- [8] D. M. Basko, I. L. Aleiner, and B. L. Altshuler, Annals of Physics **321**, 1126 (2006), cond-mat/0506617.
- [9] V. Oganesyan and D. A. Huse, Phys. Rev. B **75**, 155111 (2007), cond-mat/0610854.
- [10] M. Žnidarič, T. Prosen, and P. Prelovšek, Phys. Rev. B **77**, 064426 (2008), 0706.2539.
- [11] J. Z. Imbrie, ArXiv e-prints (2014), 1403.7837.
- [12] R. Nandkishore and D. A. Huse, Annual Review of Condensed Matter Physics **6**, 15 (2015), 1404.0686.
- [13] G. Refael and E. Altman, Comptes Rendus Physique **14**, 725 (2013), 1402.6008.
- [14] D. A. Huse, R. Nandkishore, V. Oganesyan, A. Pal, and S. L. Sondhi, Phys. Rev. B **88**, 014206 (2013), 1304.1158.
- [15] D. Pekker, G. Refael, E. Altman, E. Demler, and V. Oganesyan, Physical Review X **4**, 011052 (2014), 1307.3253.
- [16] A. Chandran, V. Khemani, C. R. Laumann, and S. L. Sondhi, Phys. Rev. B **89**, 144201 (2014), 1310.1096.
- [17] R. Vasseur, A. C. Potter, and S. A. Parameswaran, Physical Review Letters **114**, 217201 (2015), 1410.6165.
- [18] K. Slagle, Z. Bi, Y.-Z. You, and C. Xu, ArXiv e-prints (2015), 1505.05147.
- [19] R. Nandkishore and A. C. Potter, Phys. Rev. B **90**, 195115 (2014), 1406.0847.
- [20] R. Vasseur, A. C. Potter, and S. A. Parameswaran, Physical Review Letters **114**, 217201 (2015), 1410.6165.
- [21] A. Chandran, I. H. Kim, G. Vidal, and D. A. Abanin, Phys. Rev. B **91**, 085425 (2015), 1407.8480.
- [22] I. H. Kim, A. Chandran, and D. A. Abanin, ArXiv e-prints (2014), 1412.3073.
- [23] V. Ros, M. Müller, and A. Scardicchio, Nuclear Physics B **891**, 420 (2015), 1406.2175.
- [24] R. Vosk and E. Altman, Physical Review Letters **110**, 067204 (2013), 1205.0026.
- [25] M. Serbyn, Z. Papić, and D. A. Abanin, Physical Review Letters **111**, 127201 (2013), 1305.5554.
- [26] M. Serbyn, Z. Papić, and D. A. Abanin, Physical Review Letters **110**, 260601 (2013), 1304.4605.
- [27] D. A. Huse, R. Nandkishore, and V. Oganesyan, Phys. Rev. B **90**, 174202 (2014), 1305.4915.
- [28] C. Dasgupta and S.-k. Ma, Phys. Rev. B **22**, 1305 (1980).
- [29] R. N. Bhatt and P. A. Lee, Phys. Rev. Lett. **48**, 344 (1982).
- [30] D. S. Fisher, Phys. Rev. Lett. **69**, 534 (1992).
- [31] D. S. Fisher, Phys. Rev. B **50**, 3799 (1994).
- [32] D. S. Fisher, Phys. Rev. B **51**, 6411 (1995).
- [33] R. Vasseur, A. J. Friedman, S. A. Parameswaran, and A. C. Potter, ArXiv e-prints (2015), 1510.04282.
- [34] A. C. Potter, T. Morimoto, and A. Vishwanath, arXiv:1602.05194 [cond-mat] (2016).
- [35] Error bars denote 1 standard deviation errors. All error estimates include the statistical error due to a finite number of disorder samples. Critical exponent error estimates also include an estimate of the error due to finite system sizes.
- [36] S. Gopalakrishnan, M. Mueller, V. Khemani, M. Knap, E. Demler, and D. A. Huse, ArXiv e-prints (2015), 1502.07712.
- [37] D. Fattal, T. S. Cubitt, Y. Yamamoto, S. Bravyi, and I. L. Chuang, eprint arXiv:quant-ph/0406168 (2004), quant-ph/0406168.
- [38] G. Refael and J. E. Moore, Physical Review Letters **93**, 260602 (2004), cond-mat/0406737.
- [39] J. H. Bardarson, F. Pollmann, and J. E. Moore, Physical Review Letters **109**, 017202 (2012), 1202.5532.
- [40] K. Slagle, *SBRG*, <https://github.com/kjslag/SBRG> (2016).
- [41] See Appendix B for details of the SBRG method.

Appendix A: Many Body Localization

A Hamiltonian is said to be fully many body localized (MBL) if all eigenstates in the many-body spectrum are localized [12]. It is believed that there exists a finite local unitary transformation U that can diagonalize the MBL Hamiltonian H :

$$H_{\text{eff}} = UHU^\dagger \quad (\text{A1})$$

$$= \sum_i h_i^{(1)} \tau_i^z + \sum_{ij} h_{ij}^{(2)} \tau_i^z \tau_j^z + \sum_{ijk} h_{ijk}^{(3)} \tau_i^z \tau_j^z \tau_k^z + \dots$$

where the τ_i^z are the LIOM. The fact that U is a finite local unitary transformation means that it can be written as a finite time evolution of a time dependent local Hamiltonian with bounded spectrum. This implies that the LIOM $U\tau_i^z U^\dagger$ must be local operators (with exponentially decaying tails). This implies that the eigenstates of an MBL Hamiltonian display an area law entanglement (Fig. 4), as opposed to the volume law seen in excited states of thermal systems. An example of such a U can be inferred from Fig. 12. Furthermore, the $h_{ijk\dots}^{(n)}$ decay exponentially with n (Fig. 3) and distance $\max(|i-j|, |i-k|, |j-k|, \dots)$. This implies that in an MBL system, the time evolution of a direct product state displays an entanglement entropy which increases only logarithmically with time [10, 26, 39], instead of linearly as in thermal systems. This implies that an MBL system can't efficiently spread entanglement, and thus can't act as its own heat bath.

1. Marginal MBL

If one observes a phase transition between two fully MBL phases, then it's possible that the critical point between them is a marginal MBL phase. A marginal MBL phase doesn't obey Eq. (A1) with the same restrictions for the unitary transformation U and coefficients $h_{ijk\dots}^{(n)}$. For example, the LIOM in the original bases $U\tau_i^z U^\dagger$ become nonlocal [1], which implies that U can't be a finite local unitary transformation. In SBRG, the unitary transformation U that is found is nonlocal and requires a time evolution that diverges logarithmically with the system size, as can be inferred from Fig. 11.

Appendix B: Spectrum Bifurcation Renormalization Group

In this work, we use the recently developed Spectrum Bifurcation Renormalization Group (SBRG) [1] to simulate the XYZ model. SBRG is similar to RSRG-X [15], and behaves similarly to RSRG-X for the models on which RSRG-X can be applied. However, SBRG differs in that it (approximately) computes the commuting local

integrals of motion (LIOM) (also known as localized-bit [27] stabilizers) of a Hamiltonian, and therefore targets the entire spectrum at once; while RSRG-X targets a specific eigenstate energy at a time. That is, given an arbitrary local Hamiltonian H written in terms of physical spins σ_i^μ , SBRG computes the unitary transformation U to a set of LIOM Pauli operators τ_i^μ such that H can be written as the sum of products of commuting τ_i^z operators with coefficients $(h_i^{(1)}, h_{ij}^{(2)}, h_{ijk}^{(3)}, \dots)$ as in Eq. (A1). The unitary transformation U is encoded using alternating C_4 transformations (see end of Appendix B 1) and small Schrieffer-Wolff perturbations (Eq. (B4)).

With this information, SBRG can efficiently compute many quantities of interest such as Edwards-Anderson spin glass order parameters, the energy spectrum, entanglement entropies, and other LIOM properties. One advantage of SBRG is that it can handle Hamiltonian terms which are arbitrary local products of sigma matrices. This should be contrasted with other real space RG schemes (such as RSRG-X [15]) which require a specific Hamiltonian that is of closed form under RG. For example, next nearest neighbor terms often are not allowed to be created by the RG step of other methods. This flexibility allows SBRG to be applied to a large class of spin systems in all dimensions, including systems with topological order and symmetry protected topological order.

However, the price paid for this generality is that the Hamiltonian is not of closed form under RG, which results in exponentially many terms generated by the RG flow. Many of these terms will need to be dropped in order to perform computations efficiently. In this work, up to 256 additional off-diagonal terms are allowed to be added during each RG step. This approximation seems to work well for systems with large disorder and deep in the fully MBL phase; but in marginal MBL phases, very large system sizes can become problematic. However, for the XYZ chain, it appears that reasonably accurate simulations can still be performed for systems of roughly 256 spins in the marginal MBL phase, and at least 10,000 spins deep in the MBL phase.

1. RG Step and Approximations

In SBRG, the Hamiltonian of a system is written as a linear combination of tensor products of Pauli matrices:

$$H = \sum_{[\mu]} h_{[\mu]} \sigma^{[\mu]} = \sum_{[\mu]} h_{[\mu]} \otimes_i \sigma^{\mu_i} \quad (\text{B1})$$

As described in Appendix A2 of [1], for each RG step, the term $h_3 \sigma^{[\mu_3]}$ with the largest coefficient h_3 is chosen to be the next local integral of motion (LIOM) since it describes the leading energy scale. However, $\sigma^{[\mu_3]}$ doesn't

yet commute with the Hamiltonian H . The Hamiltonian can be split into three parts

$$H = h_3 \sigma^{[\mu_3]} + \Delta + \Sigma$$

where Δ commutes with $\sigma^{[\mu_3]}$ while Σ anticommutes with $\sigma^{[\mu_3]}$. In order to make $\sigma^{[\mu_3]}$ into a LIOM, we must eliminate Σ . First assume that

$$|\Sigma| \ll h_3 \quad (\text{B2})$$

$$\max_{\Delta_0 \in \Delta, [\Sigma, \Delta_0] \neq 0} |\Delta_0| \ll h_3 \quad (\text{B3})$$

where $|\Sigma| \equiv \sqrt{2^{-L} \text{Tr}(\Sigma \cdot \Sigma^\dagger)}$ and $\max_{\Delta_0 \in \Delta, [\Sigma, \Delta_0] \neq 0} |\Delta_0|$ is the absolute value of the largest pauli matrix coefficient of all terms in Δ that don't commute with Σ . Fig. 8 provides evidence that these assumptions are valid. (RSRG-X depends on a similar set of assumptions.) With these assumptions, a Schrieffer-Wolff transformation can be performed in order to eliminate the off-diagonal component Σ to order $O(h_3^{-2})$:

$$\begin{aligned} S &= \exp\left(-\frac{1}{2h_3} \sigma^{[\mu_3]} \Sigma\right) \\ &= 1 - \frac{1}{2h_3} \sigma^{[\mu_3]} \Sigma - \frac{1}{8h_3^2} \Sigma^2 + O(h_3^{-3}) \end{aligned} \quad (\text{B4})$$

$$\begin{aligned} H &\rightarrow H' = S^\dagger H S \\ &= h_3 \sigma^{[\mu_3]} + \Delta + \frac{1}{2h_3} \sigma^{[\mu_3]} \Sigma^2 \\ &\quad + \frac{1}{2h_3} \sigma^{[\mu_3]} [\Sigma, \Delta] + O(h_3^{-2}) \end{aligned} \quad (\text{B5})$$

The first approximation (Eq. (B2)) allows the unitary S to be expanded and implies that the third term in H is small: $\frac{1}{2h_3} \sigma^{[\mu_3]} \Sigma^2 \sim O(h_3^{-1})$. Although the first three terms of H' (Eq. (B5)) commute with $\sigma^{[\mu_3]}$, the final term ($\frac{1}{2h_3} \sigma^{[\mu_3]} [\Sigma, \Delta]$) does not. This term must be removed since it's $O(h_3^{-1})$, which is the leading order in the new terms that are generated by the RG step. However, this term can be ignored since another unitary transformation can eliminate it at the expense of only $O(h_3^{-2})$ terms:

$$\begin{aligned} H' &\rightarrow H'' = U^\dagger H U \\ &= h_3 \sigma^{[\mu_3]} + \Delta + \frac{1}{2h_3} \sigma^{[\mu_3]} \Sigma^2 + O(h_3^{-2}) \end{aligned} \quad (\text{B6})$$

The second approximation (Eq. (B3)) is used to claim that the last term in Eq. (B5) is indeed $O(h_3^{-1})$.

Thus, $\sigma^{[\mu_3]}$ is a LIOM of H'' at order $O(h_3^{-2})$ if we can assume Eq. (B2) and B3. In Fig. 8 we show that these appear to be safe and controlled approximations for sufficiently large Γ in the critical phase. (The approximations are even better in the spin glass phase.) The first approximation (Eq. (B2)) gets better under RG flow, while the second (Eq. (B3)) does not show a clear trend. If the second approximation is actually getting

worse under RG, this might suggest that the critical phase in the XYZ model is actually thermal.

Now that $\sigma^{[\mu_3]}$ commutes with the Hamiltonian, we may want to perform a change of basis $\sigma^{[\mu_3]} \rightarrow \tau_j^3$. Any integer j can be used as long as it hasn't been used before. E.g. j could be chosen to indicate the RG step number, or the rough position of $\sigma^{[\mu_3]}$ on the lattice. In practice, it is convenient to use the same Hilbert space for σ and τ . This can be done by rotating $\sigma^{[\mu_3]} \rightarrow \sigma_j^3$ using a unitary transformation composed of one or two C_4 transformations $\exp\left(\frac{i\pi}{4} \sigma^{[\mu]}\right)$ as described in [1].

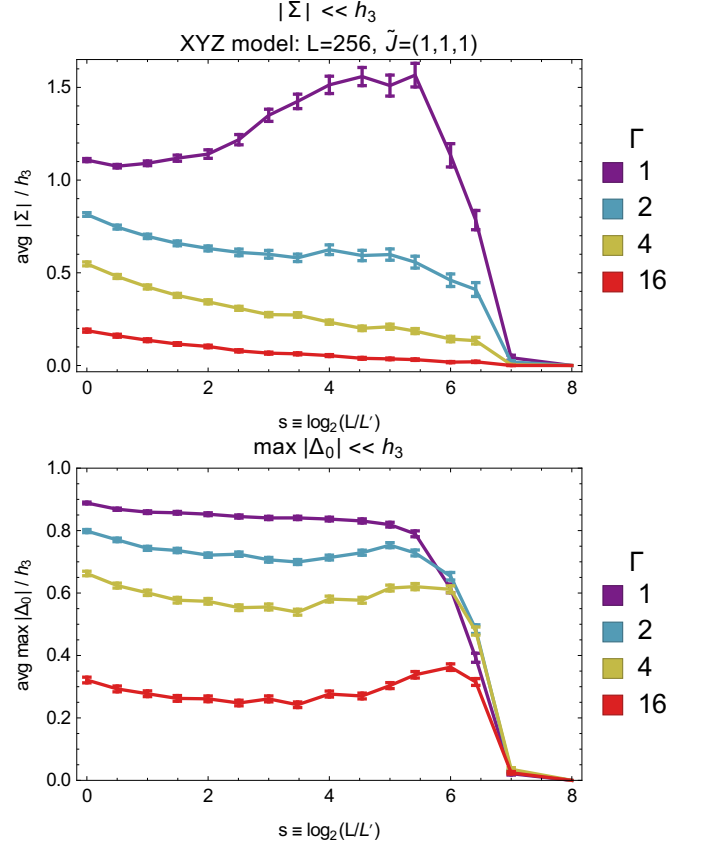


FIG. 8: Disorder average of $|\Sigma|/h_3$ (Eq. (B2)) (top) and $\max|\Delta_0|/h_3$ (Eq. (B3)) (bottom) vs amount of RG flow $s \equiv \log_2(L/L')$ for different amounts of disorder Γ where $L = 256$ is the system size and L' is the number of remaining spins. These are the small parameters used in the approximations Eq. (B2) and B3. Data is shown at the critical point $\tilde{J}_x = \tilde{J}_y = \tilde{J}_z = 1$; away from this point, these approximations are even better. As the disorder Γ increases, the plotted values get arbitrarily small, suggesting that these approximations can be controlled by Γ . In addition, the first approximation (top) gets better under RG flow (for large Γ); the second (bottom) does not show a clear trend. Similar to Fig. 3, the large Γ data in this plot can also be collapsed to a single curve if $f(y) = y^{1/\Gamma}$ is applied to the data, which shows that $|\Sigma| \sim \max|\Delta_0| \sim e^{-\Gamma}$ decreases exponentially as Γ increases. (error bar details: [35])

2. Edwards-Anderson Correlator via SBRG

Given a Hamiltonian H , SBRG calculates the Schrieffer-Wolff transformation $S_{\text{tot}} = \prod S_j$ (Eq. (B4)) that rotates (Eq. (B8)) the Hamiltonian into a basis with LIOM $\sigma_j^{[\mu_3]}$. Before applying S_{tot} , $\sigma_j^{[\mu_3]}$ are only approximate LIOM of H .

We want to calculate the energy averaged Edwards-Anderson correlator of an operator Q :

$$\text{avg}\langle Q \rangle^2 \equiv \frac{1}{N_E} \sum_E \langle E|Q|E \rangle^2 \quad (\text{B7})$$

To do this, we will apply the Schrieffer-Wolff transformation to both $\sigma^{[\mu]}$ and $|E\rangle$:

$$H \rightarrow \tilde{H} \equiv S_{\text{tot}}^\dagger H S_{\text{tot}} \quad (\text{B8})$$

$$|E\rangle \rightarrow |\tilde{E}\rangle \equiv S_{\text{tot}}^\dagger |E\rangle \quad (\text{B9})$$

$$\begin{aligned} Q \rightarrow \tilde{Q} &\equiv S_{\text{tot}}^\dagger Q S_{\text{tot}} \\ &= \sum_{[\mu]} q_{[\mu]} \sigma^{[\mu]} \end{aligned} \quad (\text{B10})$$

for some set of coefficients $q_{[\mu]}$. Now every $\sigma_j^{[\mu_3]}$ takes a definite value for every energy eigenstate $|\tilde{E}\rangle$ of \tilde{H} : $\sigma_j^{[\mu_3]} = \pm 1$. This implies that $\langle \tilde{E} | \sigma^{[\mu]} | \tilde{E} \rangle = \pm 1$ if $\sigma^{[\mu]}$ commutes with all $\sigma_j^{[\mu_3]}$, otherwise it's zero. Thus

$$\begin{aligned} \text{avg}\langle Q \rangle^2 &= \frac{1}{N_E} \sum_E \langle \tilde{E} | \tilde{Q} | \tilde{E} \rangle^2 \\ &= \frac{1}{N_E} \sum_E \sum_{[\mu]} \langle \tilde{E} | q_{[\mu]} \sigma^{[\mu]} | \tilde{E} \rangle^2 \\ &= \sum_{[\mu]} \begin{cases} q_{[\mu]}^2 & \sigma^{[\mu]} \text{ commutes with all } \sigma_j^{[\mu_3]} \\ 0 & \text{otherwise} \end{cases} \end{aligned} \quad (\text{B11})$$

In the second line, we were able to pull the $\sum_{[\mu]}$ out of $\langle \tilde{E} | \dots | \tilde{E} \rangle^2$ because cross terms cancel after the energy average. Thus, the energy averaged Edwards-Anderson correlator can be calculated from the coefficients $q_{[\mu]}$ of \tilde{Q} (Eq. (B10)).

3. Algorithm and Implementation Details

Unfortunately, the Schrieffer-Wolff transformation generates an exponentially large number of terms in Σ^2 in Eq. (B6) and \tilde{Q} in Eq. (B10). Thus, one must drop terms. In this work, for each Schrieffer-Wolff transformation, we keep the 256 largest additional terms in Σ^2 and 32 largest additional terms in \tilde{Q} .

Most operators $\sigma^{[\mu]}$ in the Hamiltonian will be local. Thus, it is important to make use of this locality when implementing SBRG. With this optimization, the CPU

time for an SBRG simulation of a Hamiltonian in an MBL phase scales linearly (up to log corrections) with system size.

For this work, each $L = 256$ disorder realization data point took a couple minutes of CPU time. However, reasonable data is achievable with only 1/8th as many additional terms in Σ^2 and \tilde{Q} , for which a simulation only takes several seconds. The SBRG data used in this paper was calculated in roughly two weeks on a quad-core i7-3720QM underclocked to 2GHz. The SBRG data included 1024 disorder realizations for each data point. However, reasonable data was attainable with less (~ 100) disorder realizations and additional terms, for which only a few hours of simulation time is necessary.

For this work, the Haskell programming language was used to implement SBRG in roughly 1000 lines of code, and the implementation has been published to github [40]. Haskell was chosen because it could produce fast code (potentially faster than C++ due to very efficient garbage collection) while requiring the smallest amount of developer time compared to other languages. Development time was minimized using Haskell because Haskell is very good at dealing with complicated data structures, which were necessary for making use of the locality of operators mentioned above. This is a result of Haskell's strong type system, automatic garbage collection, functional programming paradigm, and high amount of expressiveness.

Random numbers were generated using a combined linear congruential generator (System.Random.StdGen in Haskell) with period 2^{61} , which is much larger than the number of random numbers used in this work, which was roughly 2^{29} .

Appendix C: XYZ Model Details

1. Disorder Distribution

SBRG is a numerical method which relies on large disorder for accuracy. For this reason, it is important that we choose a disorder distribution with very large randomness. For the XY ($J_z = 0$) and XXZ ($J_{i,x} = J_{i,y}$) spin chains, it has been shown that with large disorder, $J_{i,\mu}$ flows to a power law distribution [30, 31] with a probability distribution function (PDF) equal to

$$\text{PDF}(J_{i,\mu}) = \frac{1}{\Gamma J_{i,\mu}} \left(\frac{J_{i,\mu}}{J_\mu} \right)^{1/\Gamma}, \quad J_{i,\mu} > 0 \quad (\text{C1})$$

where Γ controls the strength of the disorder, with larger Γ corresponding to stronger disorder. It's useful to define $\beta_{i,\mu} \equiv -\ln \frac{J_{i,\mu}}{J_\mu} \geq 0$. With this definition, $\beta_{i,\mu}$ follows an exponential distribution with a mean and standard deviation (as in Eq. (1)) equal to Γ :

$$\text{PDF}(\beta_{i,\mu}) = \Gamma^{-1} e^{-\beta_{i,\mu}/\Gamma}, \quad \beta_{i,\mu} > 0 \quad (\text{C2})$$

It's also useful to define $\tilde{J}_{i,\mu}$ by $J_{i,\mu} \equiv \tilde{J}_{i,\mu}^\Gamma$. With this definition, $\tilde{J}_{i,\mu}$ is uniformly distributed in $[0, \tilde{J}_\mu]$ where $J_\mu \equiv \tilde{J}_\mu^\Gamma$:

$$\text{PDF}(\tilde{J}_{i,\mu}) = \tilde{J}_\mu^{-1} \quad , \quad 0 < \tilde{J}_{i,\mu} < \tilde{J}_\mu \quad (\text{C3})$$

We therefore let $J_{i,\mu}$ follow the above (equivalent) distributions so that we can effectively probe closer to the infinite system size limit while using the same physical system size. (We assume that the disorder becomes stronger under RG in the large disorder limit.) We will show results for $\Gamma = 4$ because this is the smallest Γ for which SBRG agrees well with exact diagonalization on small lattices (data not shown in this paper), and for which our approximations appear to be safe (see Appendix B1 and D, and Sec. III B).

2. Tuning Parameters

We use \tilde{J}_μ as tuning parameters instead of J_μ because \tilde{J}_μ are better behaved at large disorder Γ . For example, our phase diagram in Fig. 1 would depend strongly on Γ if J_μ were used as tuning parameters instead of \tilde{J}_μ . However, when \tilde{J}_μ are used as tuning parameters, the phase diagram has little dependence on Γ when Γ is large; and this allows the large disorder limit to be well defined.

A simple calculation makes this more transparent. If $P(J_{i,\mu} > J_{i,\nu})$ is the probability that $J_{i,\mu} > J_{i,\nu}$, then $P(J_{i,\mu} > J_{i,\nu}) \rightarrow \frac{1}{2}$ as $\Gamma \rightarrow \infty$ if J_μ is held constant. Thus large disorder effectively washes out the differences between different J_μ and the $J_1 = J_2 = J_3$ point effectively dominates the phase diagram if J_μ is held constant as $\Gamma \rightarrow \infty$. However, if we define $J_\mu \equiv \tilde{J}_\mu^\Gamma$ and hold \tilde{J}_μ constant instead, then $P(J_{i,\mu} > J_{i,\nu})$ is independent of Γ . This is because

$$\begin{aligned} P(J_{i,\mu} > J_{i,\nu}) &= P(\tilde{J}_{i,\mu} > \tilde{J}_{i,\nu}) \text{ since } J_{i,\mu} \equiv \tilde{J}_{i,\mu}^\Gamma \\ &= \begin{cases} \frac{r}{2} & \text{if } r < 1 \\ 1 - \frac{1}{2r} & \text{if } r > 1 \end{cases} \text{ by Eq. (C3)} \\ &\text{where } r = \frac{\tilde{J}_\mu}{\tilde{J}_\nu} = \left(\frac{J_\mu}{J_\nu}\right)^{1/\Gamma} \end{aligned}$$

Appendix D: Exact Diagonalization Study

We now study the critical point $\tilde{J}_x = \tilde{J}_y = \tilde{J}_z = 1$ using exact diagonalization to check that the critical phase is not thermal. In Fig. 9 we show the level statistic r of the XYZ model vs disorder strength Γ . For each disorder realization, the level statistic $r_n^{(a)}$ is defined as a ratio of level spacings $\delta_n^{(a)}$ [9] in a given symmetry

sector (a):

$$\begin{aligned} r_n^{(a)} &\equiv \frac{\min(\delta_n^{(a)}, \delta_{n+1}^{(a)})}{\max(\delta_n^{(a)}, \delta_{n+1}^{(a)})} \\ \delta_n^{(a)} &\equiv E_n^{(a)} - E_{n-1}^{(a)} \\ E_{n+1}^{(a)} &\geq E_n^{(a)} \end{aligned} \quad (\text{D1})$$

For our model, there are four symmetry sectors (a) which are labeled by the eigenvalues of the symmetry operators of our model: $\prod_i \sigma_i^x$ and $\prod_i \sigma_i^y$. In Fig. 9 we average over disorder realizations, level spacings n , and symmetry sectors (a). We find that with weak disorder Γ , the level statistic approaches (with increasing system size) the GOE (Gaussian orthogonal ensemble) level statistic $r_{\text{GOE}} \approx 0.53$, which is expected for a thermal system. As the disorder strength increases, the level statistic drops below the Poisson level statistic $r_{\text{Poisson}} \approx 0.39$, which suggests that the system is not thermal.

The level statistic continues below the Poisson level statistic because we use a power law distribution of coefficients in the Hamiltonian (Eq. (C1)), instead of a uniform or Gaussian distribution. This can be understood most easily in the $\tilde{J}_x = \tilde{J}_y = 0$ and $\tilde{J}_z = 1$ limit (see Fig. 9), where the Hamiltonian is already diagonal. When $\Gamma = 1$, we exactly reproduce the Poisson level statistic. However, a simple numerical calculation shows that as Γ increases, the level statistic decays to zero as a power law with increasing Γ : $r \sim 1/\Gamma$.

In Fig. 10 we show the how the entanglement scales with subsystem size. When the disorder is weak, the system displays a volume law entanglement, as expected for a thermal system. But for strong disorder, the entanglement increases very slowly with subsystem size, which suggests that the strong disorder results in either a MBL phase with area law entanglement or a marginal MBL phase with log-law entanglement. (In Fig. 4 we SBRG and large system sizes to show that the entanglement follows a log-law.) Again we see that for weak disorder Γ , the critical point is thermal, but with strong disorder the critical point does not appear to be thermal.

It is worth emphasizing that in both ED plots, a disorder strength of $\Gamma = 1$ (which corresponds to uniformly distributed random coefficients J_i) was not sufficient to prevent thermalization of the XYZ model's critical point. Therefore, considering disordered systems with only Gaussian (with $\Gamma \approx 1.1$ via Eq. (1)) or uniform disorder distributions may not always be sufficient if one is interested in observing marginal MBL critical phases. That is, similar to the XYZ model's critical point, other models may also require large Γ (defined by Eq. (1)) in order to prevent thermalizaion.

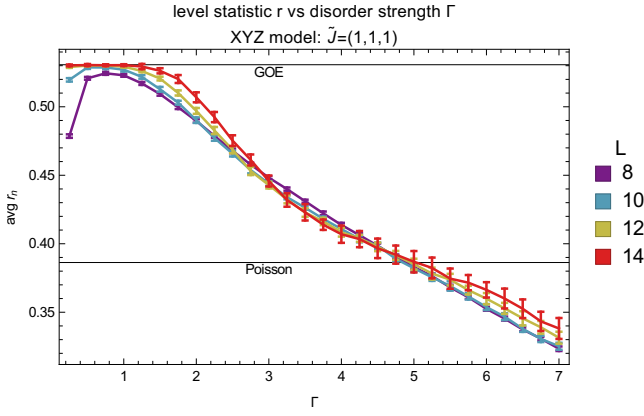


FIG. 9: Disorder and energy averaged level statistic r (Eq. (D1)) vs disorder strength Γ for different system sizes L in the XYZ spin chain with $\tilde{J}_x = \tilde{J}_y = \tilde{J}_z = 1$. With weak disorder, the system approaches GOE level statistics with increasing system size, which indicates that the system is thermal. As the disorder strength increases, the level statistic drops below the Poisson level statistic, which suggests that the system is not thermal with strong disorder. (error bar details: [35])

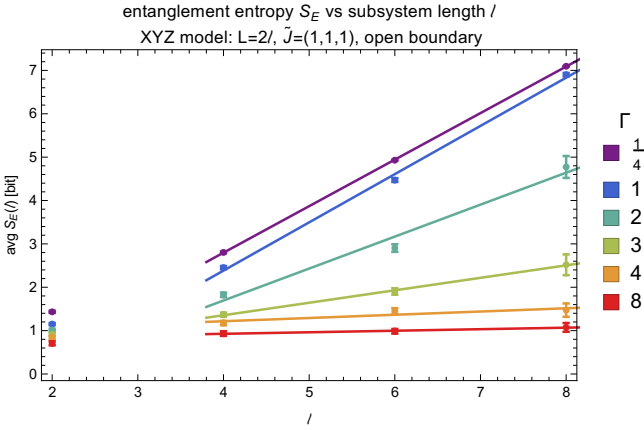


FIG. 10: Disorder and energy averaged entanglement entropy S_E [bit] ($\equiv S_E/\ln 2$) (Eq. (6)) vs subsystem length l for different disorder strengths Γ in the XYZ spin chain with $\tilde{J}_x = \tilde{J}_y = \tilde{J}_z = 1$ and system size $L = 2l$ with open boundary conditions. Each entanglement subsystem splits the system in half. We only show even l in order to avoid an even-odd effect. As the disorder strength Γ increases, the slope of the data decreases to roughly zero. This suggests a transition from a thermal phase with volume law entanglement to a non-thermal phase. (error bar details: [35])

Appendix E: Spin Glass Entanglement Entropy Calculation

Here we calculate the entanglement entropy of a subsystem A in the spin glass phase using the stabilizer rank algorithm in [1]. Deep in the spin glass phase where

J^z dominates, the LIOM are given by:

$$\tau_i^z = \sigma_i^z \sigma_{i+1}^z \text{ with } i = 1, 2, \dots, L-1 \quad (\text{E1})$$

$$\tau_L^z = \prod_{i=1}^L \begin{cases} \sigma^x & \text{if } J_x > J_y \\ \sigma^y & \text{if } J_y > J_x \end{cases}$$

Assuming $i < j$. We can see that in this case indeed $\sigma_i^z \sigma_j^z = \prod_{k=i}^{j-1} \tau_k^z$ is a product of the LIOM. Only three of the LIOM will be cut by the subsystem A , which we will take to be the sites $i, i+1, \dots, j$ where $j = i-1 + \ell$. These LIOM are $\tau_{i-1}^z, \tau_j^z, \tau_L^z$. We then “trace out degrees of freedom not in A ” by removing σ -matrices not in A :

$$\begin{array}{ccc} \tau_{i-1}^z = \sigma_{i-1}^z \sigma_i^z & \tau_j^z = \sigma_j^z \sigma_{j+1}^z & \tau_L^z = \prod_{i'} \sigma_{i'}^x \\ \downarrow & \downarrow & \downarrow \\ \hat{\tau}_{i-1}^z \rightarrow \sigma_i^z & \hat{\tau}_j^z \rightarrow \sigma_j^z & \hat{\tau}_L^z \rightarrow \prod_{i'=i}^j \sigma_{i'}^x \end{array}$$

We then consider the 3x3 anticommutivity matrix of these three $\hat{\tau}$ operators:

$$M = \begin{pmatrix} 0 & 0 & 1 \\ 0 & 0 & 1 \\ 1 & 1 & 0 \end{pmatrix}$$

where a 1 denotes anticommutivity while a 0 denotes commutivity. The entanglement entropy S_E is then given by

$$\begin{aligned} S_E &= \frac{\ln 2}{2} \text{rank} M \text{ (over } \mathbb{Z}_2) \\ &= \ln 2 \end{aligned} \quad (\text{E2})$$

where the matrix rank is calculated over the field \mathbb{Z}_2 . When one isn’t deep in the spin glass phase, the LIOM become more complicated (as in Fig. 12); more LIOM are cut by A ; and the entanglement entropy increases slightly due to additional boundary contributions which don’t depend significantly on the size of the subsystem A .

holographic RG flow
 XYZ model: $L=256$, $\tilde{J}=(1,1,1)$, $\Gamma=4$

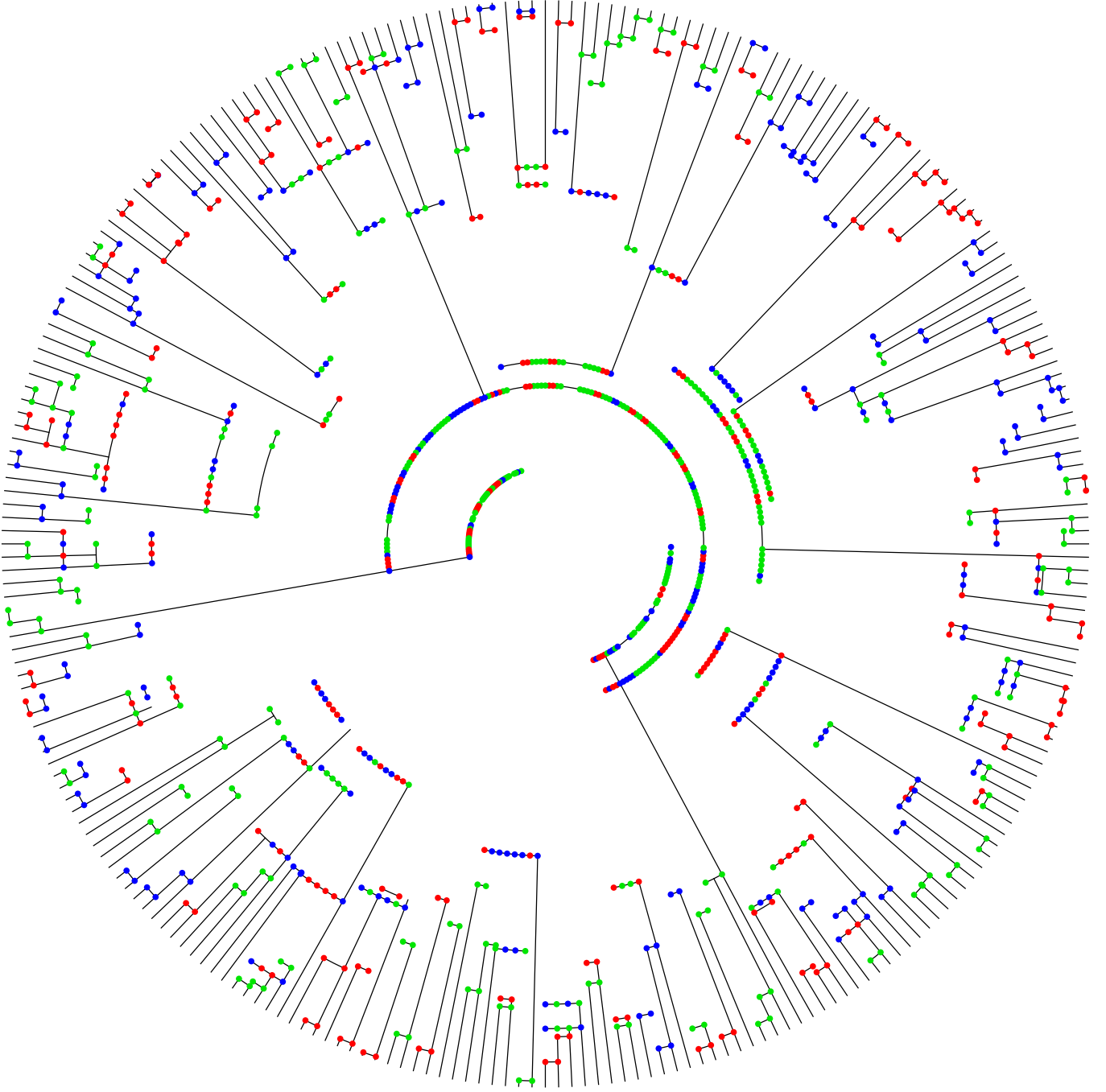


FIG. 11: Approximate RG flow and LIOM for the XYZ spin chain at the critical point $\tilde{J}_x = \tilde{J}_y = \tilde{J}_z = 1$. The initial Hamiltonian starts at the boundary of the disk, with a spin living at the end of each radial line at the edge of the disk. SBRG then performs an RG which identifies a LIOM at each step of the RG (see Appendix B 1). In the limit of large disorder, the LIOM can be approximated as a product of σ^x (red), σ^y (green), and σ^z (blue) matrices (dots connected by an arc line in the figure). Each LIOM in the figure also marks the end of a radial line to denote that a degree of freedom has been diagonalized (cf. "integrated out") at this RG step. Because we are in a marginal MBL phase, LIOM exist with sizes at every length scale, which results in the critical properties of this phase: diverging entanglement entropy (Fig. 4), power-law Edwards-Anderson correlators (Fig. 5), and long power-law range mutual information (Fig. 7).

holographic RG flow
 XYZ model: $L=256, \tilde{J}=(1,1,2), \Gamma=4$

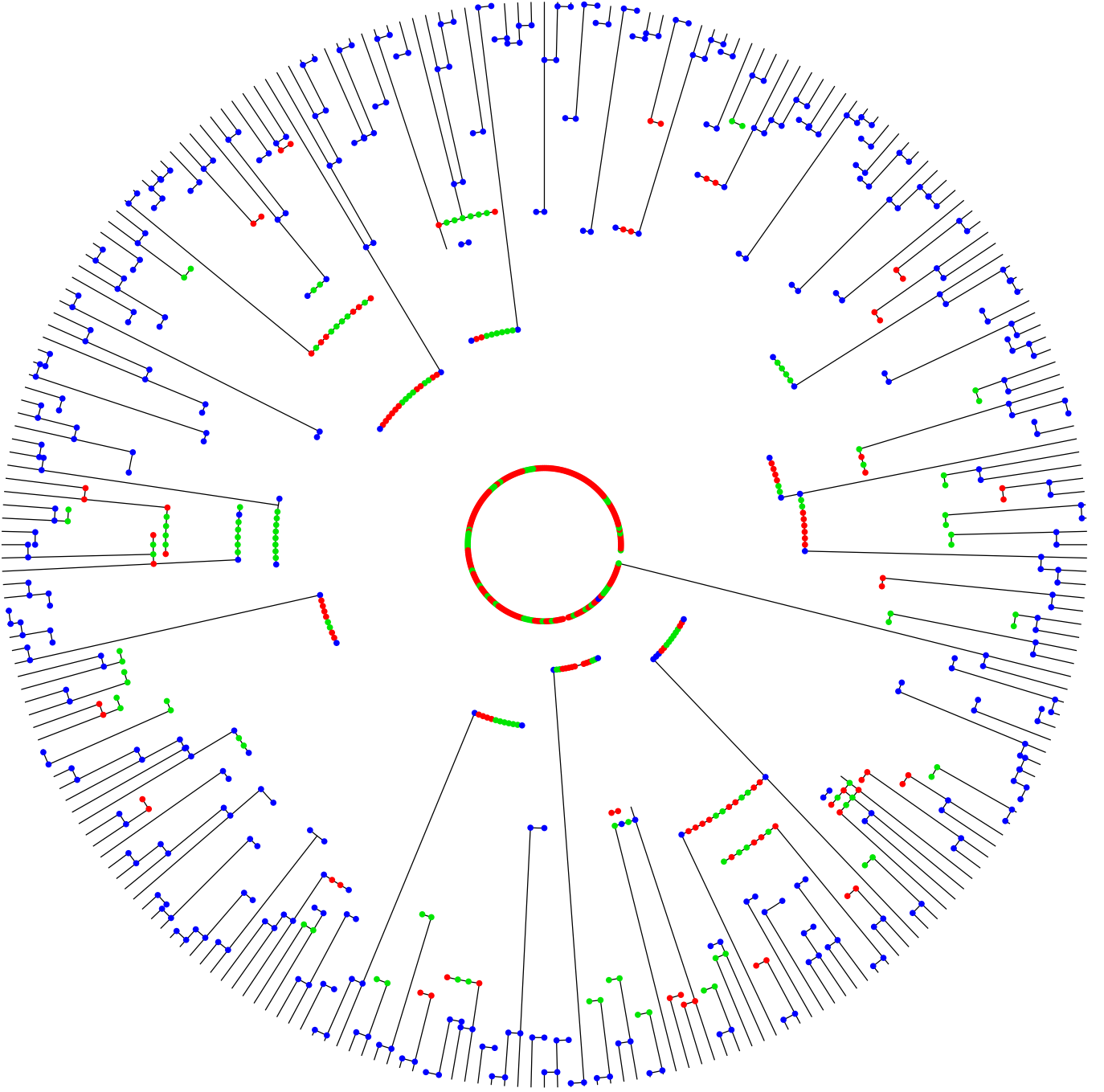


FIG. 12: Approximate RG flow and LIOM for the XYZ spin chain in the spin glass phase with $\tilde{J} = (1, 1, 2)$. (See the caption of Fig. 11.) Because we are in the spin glass phase, the LIOM are dominated by blue $\sigma^z \sigma^z$ operators. The very large integral of motion in the center is just the Z_2 spin flip symmetry $\prod_i \sigma_i^x$, which is a little messy in the figure because it has been multiplied by some of the other LIOM to obtain an operator which is still an integral of motion. This center operator is essential for the spin glass properties of this phase: finite long range Edwards-Anderson correlators (Fig. 5) and finite long range mutual information (Fig. 7).